nature photonics

Supplementary information

https://doi.org/10.1038/s41566-024-01607-8

Measuring the quantum state of photoelectrons

In the format provided by the authors and unedited

Table of Contents

1. Effect of the IR probe on the reconstructed quantum state

1.1. The effect of continuum-continuum transitions on the density matrix reconstructed with KRAKEN

As any quantum state tomography protocol, KRAKEN relies on a series of projective measurements of the initially unknown photoelectron quantum state, in order to reconstruct the density matrix. In our work, these projective measurements are performed by a pair of IR pulses that induce continuum-continuum transitions. A key assumption of the KRAKEN protocol is that the continuum-continuum transitions do not vary significantly as a function of the intermediate photoelectron energy and IR wavelength. Supplementary Fig. 1 shows the amplitude and phase of the two-photon transition matrix elements in helium for different values of the final angular momentum $L = \{0,2\}$ and total angular momentum $J = \{\frac{1}{2}, \frac{3}{2}, \frac{5}{2}\}$. Supplementary Fig. 1(a,b), shows that, for a fixed IR wavelength (800 nm), the amplitude and phase of the two-photon transition-matrix elements varies very weakly with the XUV photon energy, i.e., on the intermediate photoelectron kinetic energy. This is particularly true when considering the 140 meV bandwidth of the ionizing XUV pulse. Supplementary Fig. 1(c,d) presents the same quantities as a function of IR wavelength, for a fixed XUV photon energy (29 eV). In this case, the wavelength dependence is more important and could potentially lead to distortions of the reconstructed photoelectron quantum state.

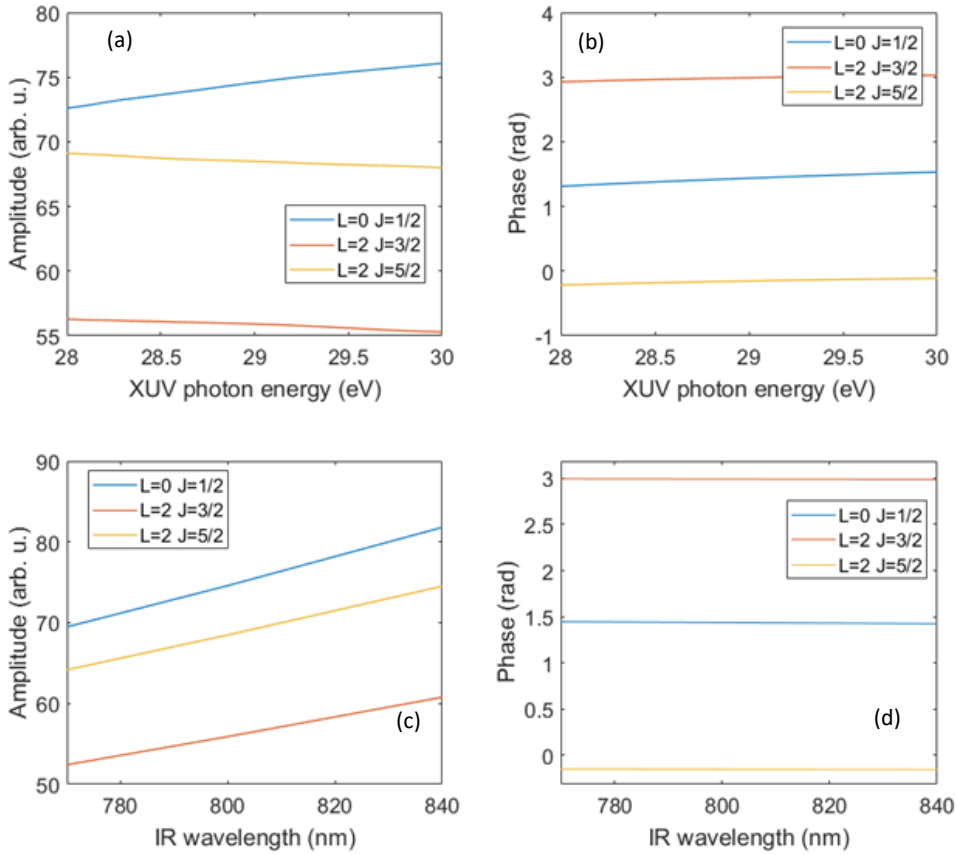

Figure 1 Amplitude (a,c) and phase (b,d) of the two-photon transition matrix elements in helium for the three final continua labeled by the angular momentum L and the total angular momentum J. The top row (a,b) shows the amplitude and phase of the matrix elements as a function of XUV photon energy for a fixed IR wavelength (800 nm). The bottom row (c,d) shows the amplitude and phase of the matrix elements as a function of IR wavelength for a fixed XUV energy (29 eV).

In order to quantify the effect of these transitions on the density matrix reconstructed with KRAKEN, in Supplementary Figs. 2 and 3, we compare the density matrix $\rho^{(1)}$ obtained from single-photon RRPAE calculations with the density matrix ρ obtained with two-photon RRPAE using the KRAKEN scheme as described in the methods section in the main text for both helium (Supplementary Fig. 2) and argon (Supplementary Fig. 3).

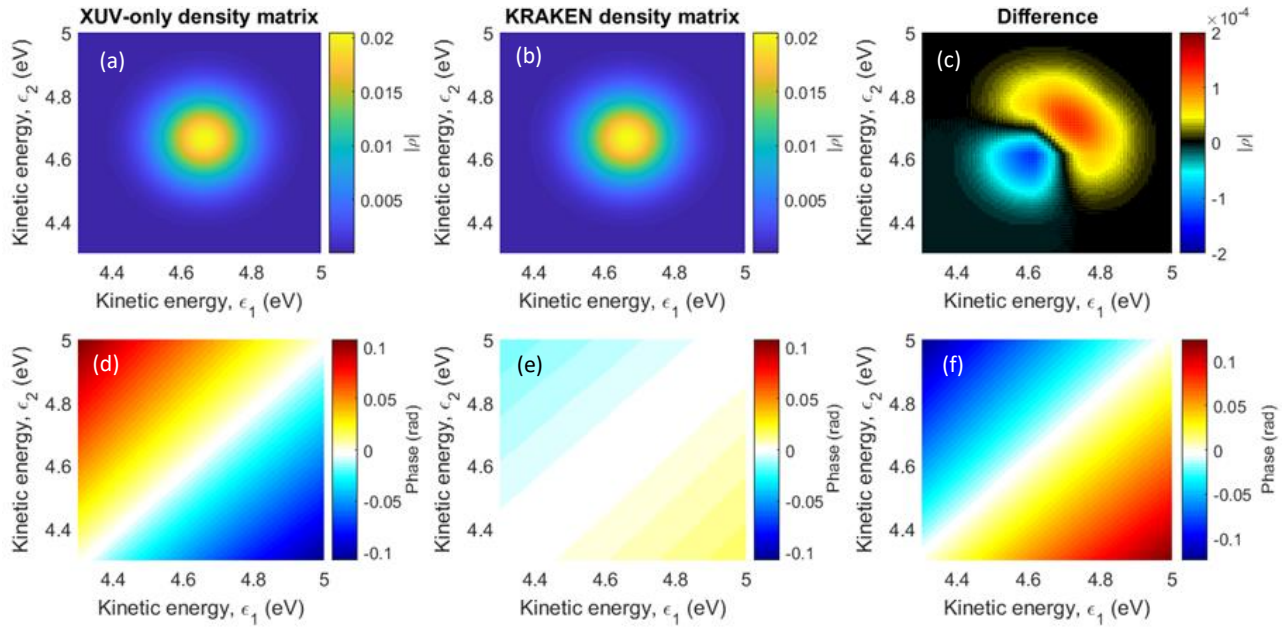

Figure 2 Comparison between the XUV-only photoelectron quantum state in helium and the one reconstructed using KRAKEN. (a,d) Amplitude (a) and phase (d) of the XUV-only photoelectron density matrix. (b,e) Amplitude and phase of the reconstructed density matrix. (c,e) Amplitude and phase of the difference between the reconstructed density matrix and the XUV-only density matrix.

In helium (Supplementary Fig. 2), the amplitudes of the two density matrices are almost identical. The difference map $\left|\rho - \rho^{(1)}\right|$ shows that the KRAKEN density matrix, ρ, is slightly shifted to higher energy due to the kinetic energy dependence of the two-photon transition, in particular the continuum-continuum transition decreasing angular momentum [see the blue curve in Supplementary Fig. 1(a)]. Nonetheless, the difference between the amplitudes of the two density matrices is two orders of magnitude smaller than that of the individual matrix elements of the density matrices. The phase of the two density matrices presents larger differences, with the density matrix ρ presenting a smaller phase variation than $\rho^{(1)}$. This can be attributed to the phase of the continuum-continuum transitions, which is positive in the case of absorption of an IR photon, while the scattering phase of the intermediate states is negative. We note that the theoretical calculations do not account for the effect of the femtochirp, which is present in the experiments and dominates over the atomic phase contributions. In addition, the phase of the density matrix does not affect the purity of the density matrix. In both cases, the density matrix is fully pure.

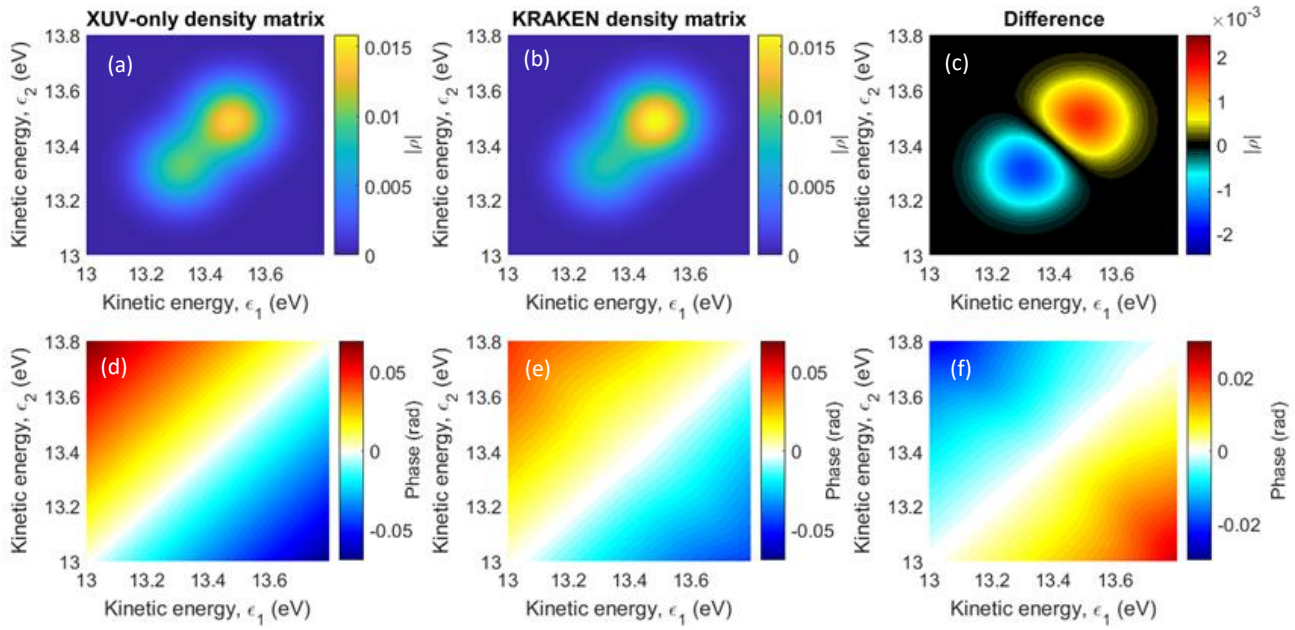

Figure 3 Same as for Fig. 2 but in the case of argon.

In argon (Supplementary Fig. 3), the amplitude of the two density matrices is slightly different, with the density matrix ρ presenting a larger population for photoelectron states associated to the ionic state $3p^5\ ^2P_{3/2}$. The small redistribution of the populations between the two density matrices, induced by the continuum-continuum transitions, can be observed more clearly in the difference map. This effect does affect the retrieved photoelectron purity. While the purity of the density matrix $\rho^{(1)}$ is 0.61, the theoretical calculations predict that the purity of the density matrix retrieved with the KRAKEN protocol is slightly higher (0.66) as a result of the redistribution of photoelectron populations associated to the two ionic states. This theoretical result is in remarkable agreement with the purity obtained experimentally. In the case of argon, contrary to helium, we observe a smaller difference in the phase of the elements of the two density matrices. This can be attributed to the fact that the continuum-continuum transitions vary more weakly with kinetic energy and wavelength at higher kinetic energy.

We conclude that, in our work, the continuum-continuum transitions do not strongly affect the results of the KRAKEN reconstruction. This approximation is better for photoelectrons with high kinetic energy. We also note that continuum-continuum transitions have been studied in detail in the past [59]. In atoms, these transitions are to a large extent universal and can be accurately computed theoretically. This could be used to correct the phase of the reconstructed density matrix, however, this lies beyond the scope of this work.

1.2. The effect of the IR spectral width

It is essential for KRAKEN measurements that the IR pulses are spectrally narrow to ensure high spectral selectivity. In practice, if the pulses are too short, two problems will arise. First, the two-photon photoelectron signal will be broadened, resulting in an effect similar to that of the convolution with the spectrometer response [60]. Second, the cross-correlation signal between XUV and IR will be shorter, which means in the Fourier domain, that the peaks will be broader. This can result, in the case of spectrograms with a small $\delta\omega$, in a contamination, in the Fourier

domain, of the peak at $\delta\omega$ by the peak at 0ω, as shown in Supplementary Fig. 4 for two different IR bandwidths and different values of $\delta\omega$. In Supplementary Fig. 4 (c,d), due to the contamination from the 0ω, the purity will be overestimated. This would result in a reconstructed density matrix with a purity that is larger than one, which is unphysical.

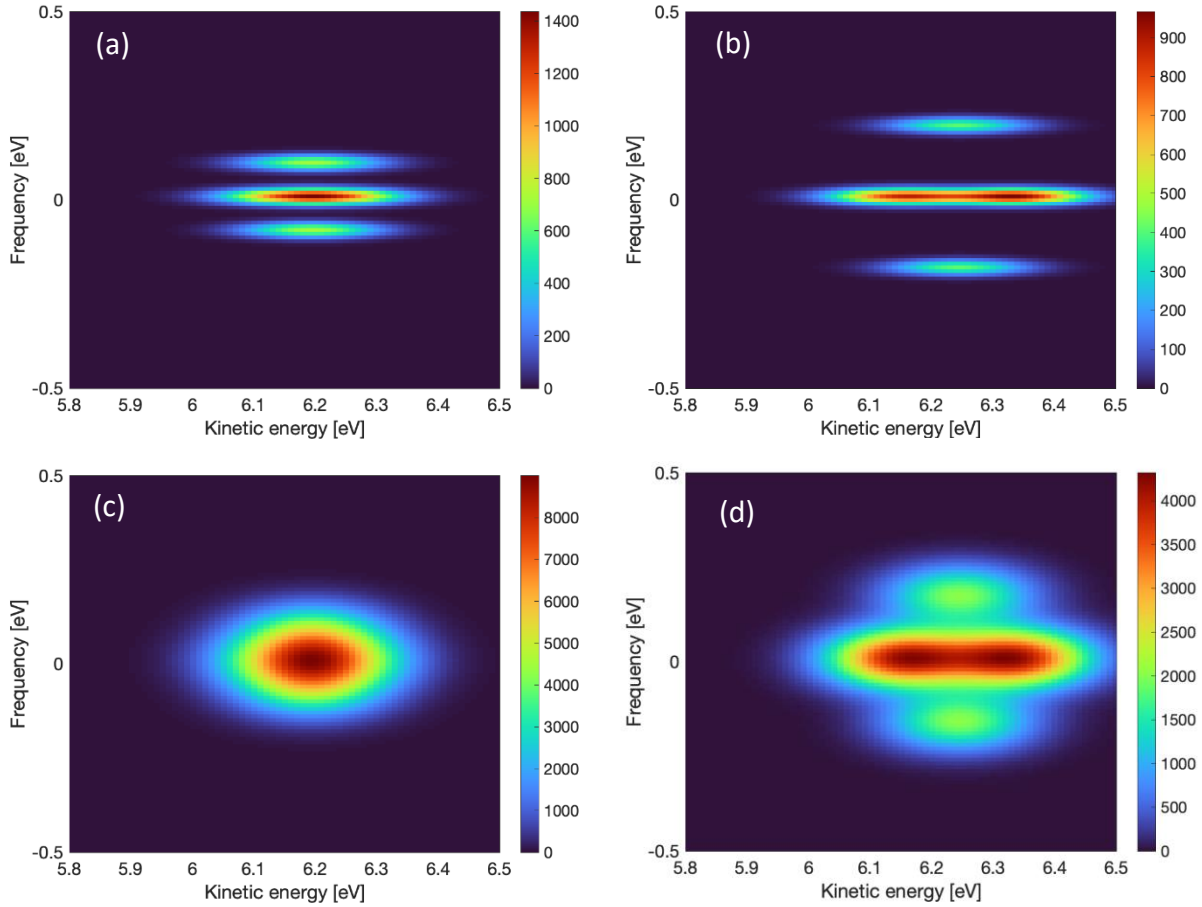

Figure 4 Effect of the IR bandwidth on the frequency resolution of the energy-resolved Fourier transform of the KRAKEN spectrograms for a δω=10 meV (a,c) and δω=20 meV (b,d). The IR bandwidth (FWHM) in (a,b) is 8.6 meV (≈110 fs), while for (c,d) it is 66 meV (≈28 fs). These simulations are performed in helium.

2. Data analysis

2.1. Fitting

First, the populations (diagonal elements of the density matrix) were extracted from the scan with one slit ($\delta\omega = 0$). As expected, the spectrograms do not exhibit oscillations. However, due to the temporal envelopes of the XUV and IR fields, the photoelectron signal varies according to the cross-correlation trace between the two fields. For each final kinetic energy, we fitted the delay-dependent photoelectron yield according to

$$S(E,\tau) = A(E)\exp[-(\tau-\tau_0)^2/2\sigma^2\,],$$

where τ_0 is the zero delay, σ is the temporal width of the autocorrelation function, and $A(E)$ is the amplitude that corresponds to the populations.

In a second step, the spectrograms with two slits in the probe arm ($\delta\omega \neq 0$) were analyzed. For each energy bin the mean value of the oscillations was subtracted. In this case, due to the two paths leading to the same final energy, the obtained photoelectron signal oscillates and was fitted with

$$S(E,\tau) = \exp[-(\tau-\tau_0)^2/2\sigma^2\,]\{A_{\delta\omega}(E)\cos[\delta\omega(\tau-\tau_0)-\varphi_{\delta\omega}(E)]\},$$

where $A_{\delta\omega}(E)$ is the amplitude of the oscillations, which is proportional to the coherences of the density matrix, and $\varphi_{\delta\omega}(E)$ is the phase of the oscillations. In this step, the parameter σ was not fitted (we set it to the value obtained from the fit of the populations), while τ_0 was allowed to vary to account for possible drifts of the delay from one scan to the other. The uncertainty of the fit was recorded and used in the Bayesian estimation.

2.2. Amplitude normalization

The amplitude of the interference signal that is measured in KRAKEN is proportional to the product of two-photon transition amplitudes associated to the two different probe frequencies, where each transition amplitude is the product of the XUV and IR field amplitudes and the transition matrix elements. Since the intensity of the XUV and IR pulses can be different from one spectrogram to the next, it is necessary to rescale them by the intensity of the pump and probe pulses. To do so, the measured oscillation amplitudes $A_{\delta\omega}^{(raw)}$ were normalized according to

$$A_{\delta\omega}(\epsilon) = \frac{A_{\delta\omega}^{(raw)}(\epsilon)}{I_{XUV}\sqrt{\alpha_{\omega1}I_{\omega1}\alpha_{\omega2}I_{\omega2}}},$$

where $I_{\omega1}$ and $I_{\omega2}$ are the spectral intensities of the two IR spectral components, which were measured with an IR spectrometer, and I_{XUV} is the intensity of the XUV pump, obtained from the measurement of the intensity of the photoelectron peak associated with absorption of harmonic 19. The factors $\alpha_{\omega1}$ and $\alpha_{\omega2}$ account for the wavelength-dependent response function of the IR spectrometer. The intensities $I_{\omega1}$, $I_{\omega2}$, and I_{XUV} were obtained by integration of the width of the corresponding photon or photoelectron peak. We note that this normalization only ensures the correct scaling between the different subdiagonals. An additional global scaling factor was applied to all the amplitudes $A_{\delta\omega}(\epsilon)$ to ensure that the reconstructed density matrix fulfils $\mathrm{tr}(\rho) = 1$.

2.3. Correction of energy shifts

In the experiments, as the spectral separation $\delta\omega$ between the two components of the IR field was varied, the kinetic energy of the two-photon electron signal moved accordingly. To reconstruct the density matrix, we used the kinetic energy of the photoelectron peak obtained for $\delta\omega = 0$ as the reference and we shifted the kinetic energy of the two-photon electron signal obtained for $\delta\omega \neq 0$. We observed that, in addition to the trivial energy shift induced by the change of $\delta\omega$, small differences in the ponderomotive shift also had to be accounted for. Indeed, for $\delta\omega = 0$ (only one slit was open in the 4f-shaper), the intensity was approximately twice lower than for both slits open. Additionally, due to the wavelength dependence of the IR intensity, we observed small differences in the ponderomotive shift for different spectrograms. The estimated values of the ponderomotive shifts ΔE_p are presented in Supplementary Table 1. The decrease of ΔE_p as a function of $\delta\omega$ matches well the variation of the spectral intensity of the different IR components presented in Extended Data Fig. 1.

We note that these shifts do not affect the main observable of the experiment, namely the decay of the oscillation amplitude/coherences with increasing $\delta\omega$. However, this correction makes the convergence of the Bayesian estimation easier.

$\hbar\delta\omega$ (eV)	0	0.041	0.061	0.08	0.098	0.117	0.134
ΔE_p (eV)	0	0.07	0.07	0.03	0.03	0.03	0

Table 1 Estimated value of the ponderomotive shift ΔEp as a function of the energy separation between the two IR spectral components.

2.4. Correction of phase shifts

The delay τ_0 varied slightly for the different subdiagonal measurements and thus led to different phase offsets from one measurement to the next. In this work, the phase of the density matrix was dominated by the intrinsic linear chirp of harmonic 19 [61], which led to a phase variation across the different subdiagonals. If $\tau_0 = 0$, $\varphi_{\delta\omega}(E)$ should cross 0 at the maximum of $A_{\delta\omega}$ for all subdiagonals. Therefore, the delay-induced phase shift was corrected by shifting the measured phases so that $\varphi_{\delta\omega}(E)$ is zero at the maximum of $A_{\delta\omega}$. The phase-shifts corrections do not carry any information about the system but, as for the energy shift, they ensure a better convergence of the Bayesian estimation. We also note that the phase plays no role for the characterization of the purity of the photoelectron and the electron-ion entanglement as provided in the main text.

3. Reconstruction of the continuous-variable density matrix

In order to estimate, from the measured data, the amplitude and phase of the underlying continuous-variable density matrix, we employed a Bayesian estimation approach using the Markov Chain Monte Carlo (MCMC) algorithm with the No-U-Turn Sampler from the numpyro package in Python [62].

3.1. Models

Different models can be used for the Bayesian optimization. In this work, we compared results using two of these.

In our first model, which is the one used for all the reconstructions presented in the main text, the amplitude of the estimated density matrix ρ_{est} is described using a mixture of 2-dimensional elliptical Gaussian distributions rotated by an angle $\theta = 45$ degrees with respect to the x axis of the 2D energy map. All the 2D Gaussians are centered along the main diagonal of the density matrix. The major axis X is along the main diagonal of the density matrix and determines the width of the populations, while the minor axis Y is along the anti-diagonal of the density matrix and determines the extension of the coherences along the anti-diagonal:

$$|\rho_{est}| = \sum_i A_i \exp\left\{-\left[a_i\left(x - x_{0,i}\right)^2 + 2b_i\left(x - x_{0,i}\right)\left(y - y_{0,i}\right) + c_i\left(y - y_{0,i}\right)^2\right]\right\},$$

with

$$a_i = \frac{\cos^2\theta}{2\sigma_{X,i}^2} + \frac{\sin^2\theta}{2\sigma_{Y,i}^2}, \qquad b_i = -\frac{\sin 2\theta}{4\sigma_{X,i}^2} + \frac{\sin 2\theta}{4\sigma_{Y,i}^2}, \qquad c_i = \frac{\sin^2\theta}{2\sigma_{X,i}^2} + \frac{\cos^2\theta}{2\sigma_{Y,i}^2}.$$

The width $\sigma_{X,i}$ depends on the XUV spectral width while the width $\sigma_{Y,i}$ determines the extension of the coherences on the anti-diagonal. $\sigma_{Y,i}$ is the parameter with strongest impact on the purity of the density matrix. To ensure that ρ_{est} corresponds to a physical (Hermitian) density matrix, we force the center of the Gaussians to be on the main diagonal, i.e., $x_{0,i} = y_{0,i}$. Additionally, we constrain the width $\sigma_{Y,i}$ such that $\sigma_{X,i} \geq \sigma_{Y,i}$, ensuring that the purity cannot be larger than one. The model can be modified to account for the spectrometer response function by convolving each sub-diagonal of $|\rho_{est}|$with the measured spectrometer function.

In helium, we used one 2D Gaussian, while in argon we used two. We have tested the model using a larger number of 2D Gaussians centered along the main diagonal, but we found that using one (two) Gaussians in helium (argon) was sufficient to reproduce the key features of the experiment. Furthermore, increasing the number of Gaussians in the model was not beneficial since, due to the larger number of free parameters, it led to larger uncertainties in the parameter estimation.

In order to take into account the spectrometer response of the MBES in the Bayesian estimation when comparing the prediction of the model to the measured subdiagonals, the amplitude of the predicted subdiagonal is further convolved with the measured response function, thus mimicking the broadening of the "real" photoelectron signal when measured by the MBES.

The phase of the density matrix is the sum of two contributions: the spectral phase of the ionizing radiation and the phase of the atomic transitions. In the present case, since we considered non-resonant ionization over a small energy range (<0.5 eV), the atomic contribution was negligible, and the phase of density matrix was completely dominated by the spectral phase of the ionizing radiation. The ionizing XUV pulse was generated via high-order harmonic generation such that it was intrinsically chirped [61]. Writing the spectral phase $\phi(\Omega)$ of the XUV pulse as $\phi(\Omega) = \gamma(\Omega - \Omega_0)^2$, with Ω_0 the central frequency of the XUV pulse and γ the chirp parameter, proportional to the group delay dispersion, the phase of the density matrix was modeled as

$$\arg(\rho_{est}) = \arg\left[\sum_i \mathcal{A}_i(x,y)\exp\big(-i\gamma\big[x+y-2x_{0,i}\big][x-y]\big)\right],$$

where $\mathcal{A}_i(x,y)$ is defined as

$$\mathcal{A}_i(x,y) = A_i \exp\left\{-\left[a_i\big(x-x_{0,i}\big)^2 + 2b_i\big(x-x_{0,i}\big)\big(y-y_{0,i}\big) + c_i\big(y-y_{0,i}\big)^2\right]\right\}.$$

Since the models for the amplitude and phase are interdependent, we applied the Bayesian optimization simultaneously for the amplitude and the phase. We note that, below a certain oscillation amplitude, the signal-to-noise ratio was too low to reliably extract the oscillation phase. Hence, we only used the extracted phase if the oscillation amplitude was larger than ≈ 10% of the maximum amplitude.

In the case of argon, we compared our results with a second model in which we use four 2D Gaussians. Two are centered along the main diagonal $(x_{0,1}\,,\,x_{0,1})$ and $(x_{0,2}\,,\,x_{0,2})$, while the other two are centered at the position of the corresponding coherences $(x_{0,1}\,,\,x_{0,2})$ and $(x_{0,2}\,,\,x_{0,1})$. The results of this comparison are presented in Supplementary Discussion 6.

3.2. Bayesian estimation

We defined the likelihood $p_{\text{likelihood}}(\text{data}|\text{parameters})$ that gives the conditional probability for the measurement of the data given a certain set of parameters describing the underlying density matrix. In this likelihood computation, we used the model described above and we assumed that the final observations contained additive Gaussian noise specified by the error bars of the measured data. Once the likelihood was constructed, we specified priors for the various parameters and sampled the posterior probability using Bayes rule

$$p_{\text{posterior}}(\text{data}|\text{parameters}) = \frac{p_{\text{likelihood}}(\text{data}|\text{parameters})p_{\text{prior}}(\text{parameters})}{p_{\text{evidence}}(\text{data})},$$

where $p_{\text{evidence}}(\text{data})$ is defined as

$$p_{\text{evidence}}(\text{data}) = \int p_{\text{likelihood}}(\text{data}|\text{parameters})p_{\text{prior}}(\text{parameters})\, \text{d}parameters.$$

The computation of this integral is complicated, but MCMC methods can be used to obtain an empirical posterior distribution of the parameters. MCMC allows sampling the parameter space by randomly proposing values for the parameters and accepting or rejecting them based on the likelihood. Here, rather than exploring the parameter space using a random walk, we used an approach based on the Hamiltonian Monte Carlo method, more specifically the No-U-Turns Sampler extension [62].

Physical knowledge of the system can be enforced in the MCMC algorithm via the distribution of priors. We used the least informative prior possible, a flat distribution, for all the parameters, except for the spin-orbit splitting energy, for which we chose a normal distribution centered around $\Delta\epsilon_{so}$ =177 meV with a standard deviation of 100 meV. Supplementary Table 2 summarizes the value of the priors used for A_i, $x_{0,i}$, $\sigma_{X,i}$, $\sigma_{Y,i}$, and γ.

MCMC algorithms need a warmup period at the beginning to allow the Markov chain to converge to the stationary distribution. This warmup period discards initial samples that are not representative of the desired distribution. After the warmup, the subsequent samples are considered as approximations from the target distribution. We used 200 warmup steps and collected 800 sets of parameters leading to different density matrices. The density matrices presented in the main manuscript correspond to the density matrix with the largest likelihood $p_{\text{likelihood}}$ of all the density matrices obtained after the warmup, and the reported purity corresponds to the purity of that density matrix. The error bar corresponds to the standard deviation based on the statistical distribution of purities obtained (Extended Data Fig. 5).

	A_i	$x_{0,1}$ (eV)	$x_{0,2}$ (eV)	$\sigma_{X,i}$ (eV)	$\sigma_{Y,i}$ (eV)	γ
He	Uniform $(10^{-4}, 10^{-1})$	Uniform (6.14,6.28)	-	Uniform (0.08,0.15)	Uniform (0.08, $\sigma_{X,i}$)	Uniform (-50,50)
Ar	Uniform $(10^{-3}, 10^{-1})$	Uniform (14.71,15.21)	$x_{0,1}$+ Normal (0.177,0.1)	Uniform (0.05,0.2)	Uniform (0.01, $\sigma_{X,i}$)	Uniform (-50,50)

Table 2 Prior distributions used in the MCMC algorithm. Uniform (α,β) corresponds to a uniform distribution with minimum value α and maximum value β. Normal (μ,σ) corresponds to a normal distribution with mean value μ and standard deviation σ.

4. Comparison of the experimental data in helium and argon

Supplementary Fig. 5, presents side by side the measured density matrix amplitude for helium and argon as well as the reconstructed density matrix obtained with the Bayesian estimation algorithm. The partially reconstructed density matrices measured in helium and argon [Supplementary Fig. 5 (a,b)] present clear differences. The coherences in helium extend along the anti-diagonal as much as the populations do along the main diagonal. In contrast in argon, the populations extend significantly more than the coherences along the antidiagonal. The difference between the density matrices obtained in the two atomic targets remains after the application of the Bayesian estimation algorithm to reconstruct the continuous variable density matrix [Supplementary Fig. 5 (c,d)].

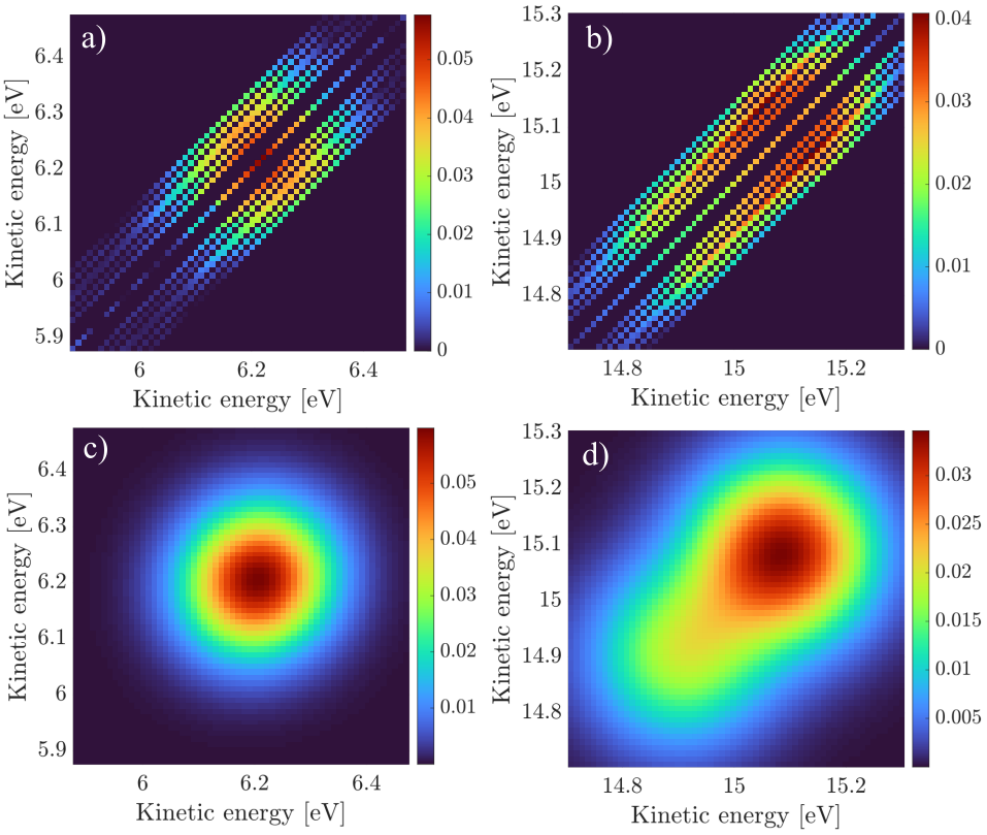

Figure 5 Comparison of the (a,b) measured and (c,d) estimated density matrices for (a,c) helium and (b,d) argon. In argon, the density matrix is obtained using the two-Gaussian model.

5. <u>Comparison of the data in argon with a pure state model</u>

It is interesting to compare the absolute value of the coherences measured at different subdiagonals with the amplitude that would be obtained if the state was pure, which is given by $|\rho(\epsilon_1, \epsilon_2)| = \sqrt{\rho(\epsilon_1, \epsilon_1)\rho(\epsilon_2, \epsilon_2)}$. Supplementary Fig. 5 presents such a comparison between the measured data (blue curves), the amplitude obtained from the Bayesian estimation (red curves), and the expected amplitude for a pure state (black curve). The red and black curves are increasingly different as δω

increases and for the furthest subdiagonal, the red curve reproduces better the measured data both qualitatively (the red curve is asymmetric, like the measured data, while the black curve is symmetric) and quantitatively. This indicates that we do indeed observe decoherence in our measurements. It is worth noting that the discrepancy between the measured data and the black curve is strongest at the center of the subdiagonals, where the coherence between the continuum states with large energy separation and associated to different ionic states is measured. In contrast, there is not much difference between the different curves at the two edges of the subdiagonal since this mostly corresponds to coherences between continuum states associated to the same ionic state.

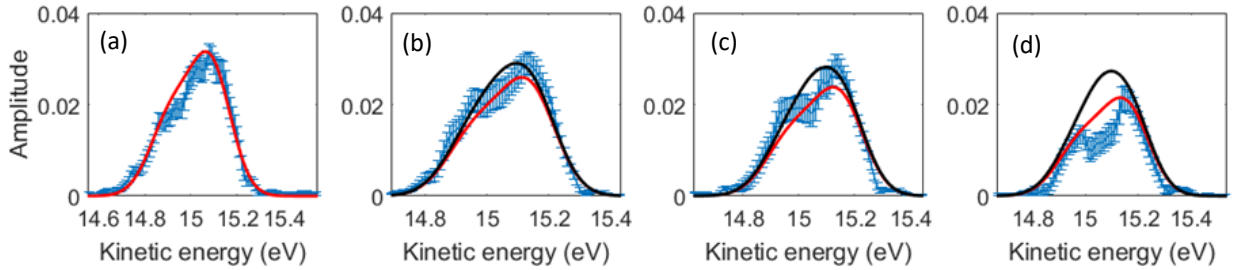

Figure 6 Comparison of the amplitude of few measured subdiagonals measured in argon (blue) with the estimated density matrix (red) as well as with the expected subdiagonal amplitude in the case of pure state (black). The experimental data is presented as the mean value with 95% confidence interval obtained from the fit (n=41 data points). a) shows the main diagonal while (b-d) show the subdiagonals corresponding to $\hbar\delta\omega$=98 meV, $\hbar\delta\omega$=117 meV, and $\hbar\delta\omega$=134 meV, respectively.

6. Phase of the density matrix

Supplementary figure 6 presents the amplitude of the measured density matrices in helium (a) and argon (d), as well as the amplitude of the corresponding density matrix obtained with the Bayesian estimation algorithm using the two-Gaussian model (b,c,e,f). The helical phase structure of the density matrix is a signature of the chirp of the ionizing radiation as discussed above. In argon, the phase variation is more complex due to the spin-orbit splitting. The observed phase variation is orders of magnitude larger than induced by the kinetic energy and wavelength dependence of the continuum-continuum phase, which, in this case, can be neglected.

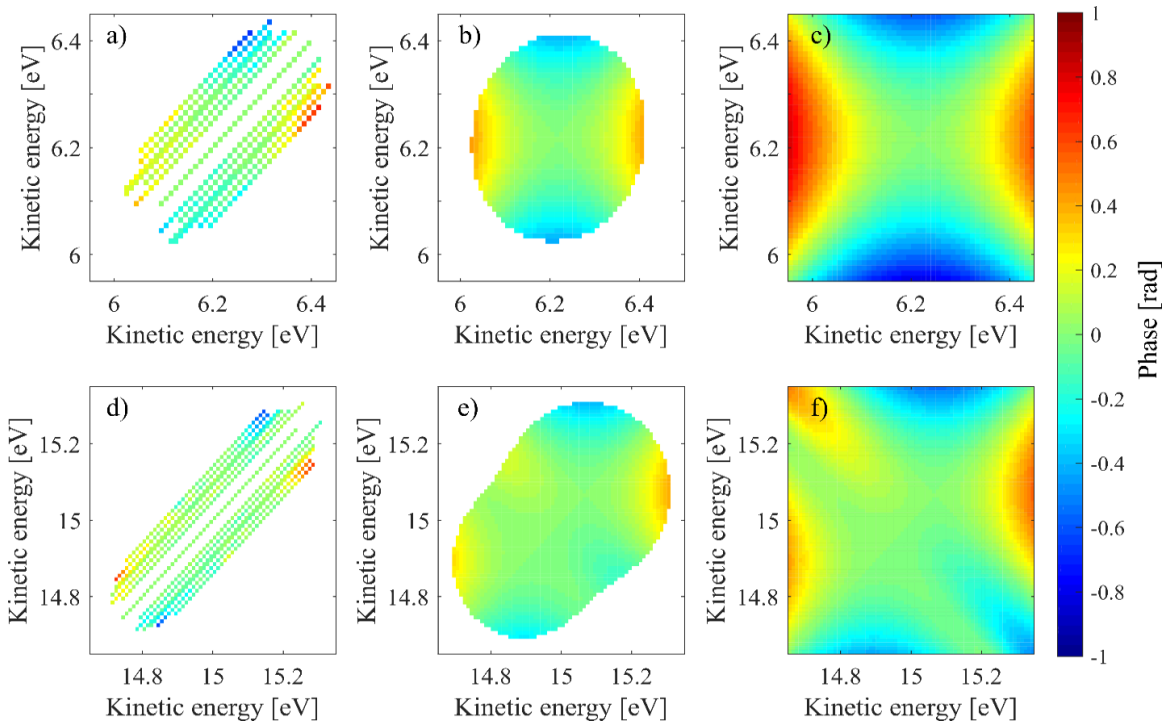

Figure 7 Phase of the density matrix of photoelectron emitted from (a-c) helium and (d-f) argon. (a,d) Phase of the measured density matrix. The phase is shown only for matrix elements with an amplitude larger than 10% of the maximum amplitude. (b,e) Phase of the estimated density matrix. To ease the comparison with (a,d), we apply the same threshold as for the raw data. (c,f) Phase of the estimated density matrix without amplitude threshold.

7. Bayesian estimation in argon

Supplementary Fig. 8 compares the amplitude and purity of the density matrices obtained in the case of argon using two-Gaussian model [Supplementary Fig. 8 (a)] and the four-Gaussian model [Supplementary Fig. 8 (b)]. Both density matrices are elongated along the main diagonal compared to the anti-diagonal, indicating a loss of coherence. The difference map presented in Supplementary Fig. 8 (c) shows that the main difference between the two retrieved density matrices is the presence of two small off-diagonal features, corresponding to two off-diagonal Gaussians added in the second model. It is interesting to note that these features are small and very narrow along the antidiagonal, indicating that the Bayesian estimation minimizes the extent of these artificially introduced coherences.

Supplementary Fig. 8 (d) presents the purity distributions obtained using the two different models. Both distributions peak around the same value of the purity, but the distribution of the four-Gaussian model has a broader distribution, extending towards higher values of the coherence. The two-Gaussian model yields a mean purity of 0.65 with a standard deviation of 0.02, while the four-Gaussian model yields a mean purity of 0.68 and a standard deviation of 0.04. In both cases, the mean value of the purity distribution is in excellent agreement with the theoretical predictions for the density matrix reconstructed using the KRAKEN scheme (more details in the section

Theoretical model). The fact that the two models give consistent results gives us confidence that our result is robust and does not significantly depend on the model used in the Bayesian estimation.

Since the predictions from the four-Gaussian model are very similar to those of the two-Gaussian model, and because the four-Gaussian model tends to minimize the impact of the artificially introduced coherences, in the main manuscript, we only present the results obtained with the two-Gaussian model.

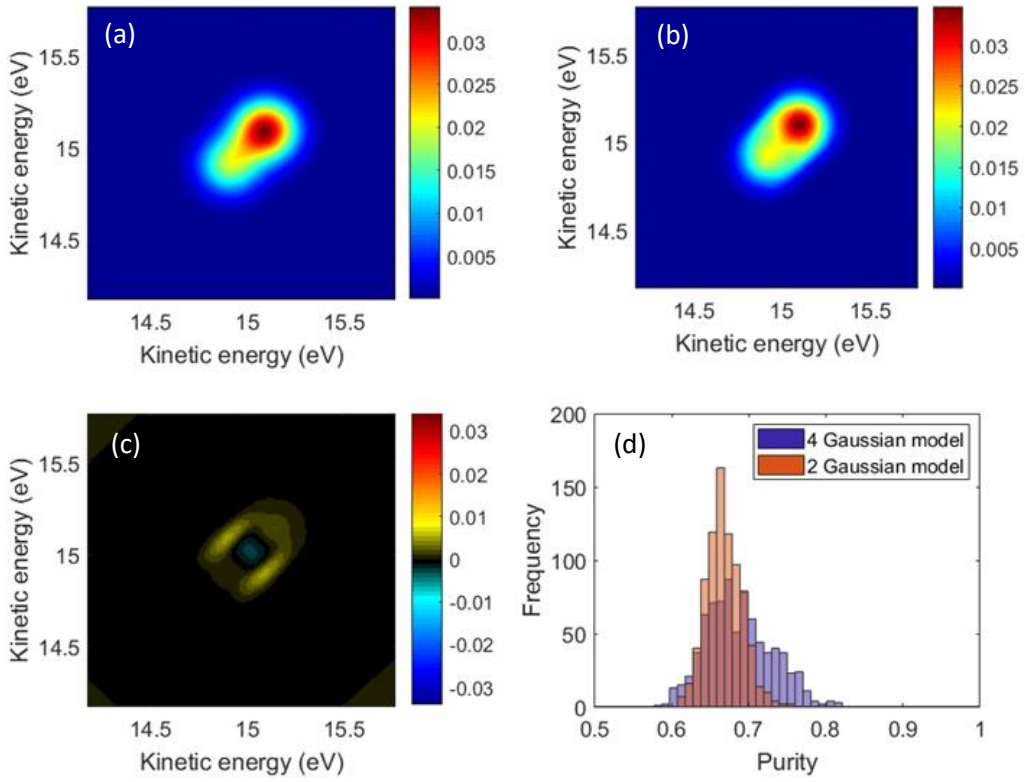

Figure 8 Density matrix amplitude obtained using the two-Gaussian model. (b) Density matrix amplitude obtained using the four-Gaussian model. (c) Difference map of density matrix amplitudes obtained with the four-Gaussian model and the two-Gaussian model. (d) Comparison of the purity distributions obtained using the two- and four-Gaussian models.

We further verify that the results obtained from the Bayesian estimation are not the result of a bias in the models. To do so, we apply the Bayesian estimation algorithm on the data using only the measurements of the populations and discarding the measurements of the coherences. Supplementary Fig. 9 shows the purity distributions obtained from both models. In both cases, the purity distribution is extremely broad. In the case where only two Gaussians are used, the model is slightly biased, generating density matrices with rather low purity. Interestingly the result that we obtain using all the diagonals lies at the edge of this distribution. We can thus confirm that our models are not strongly biased and that purity distributions presented in Extended Data Fig. 4 cannot be explained by a bias of our model. This result demonstrates that, without the measurement of the subdiagonals using KRAKEN, it is not possible to determine accurately experimentally the purity of the photoelectrons.

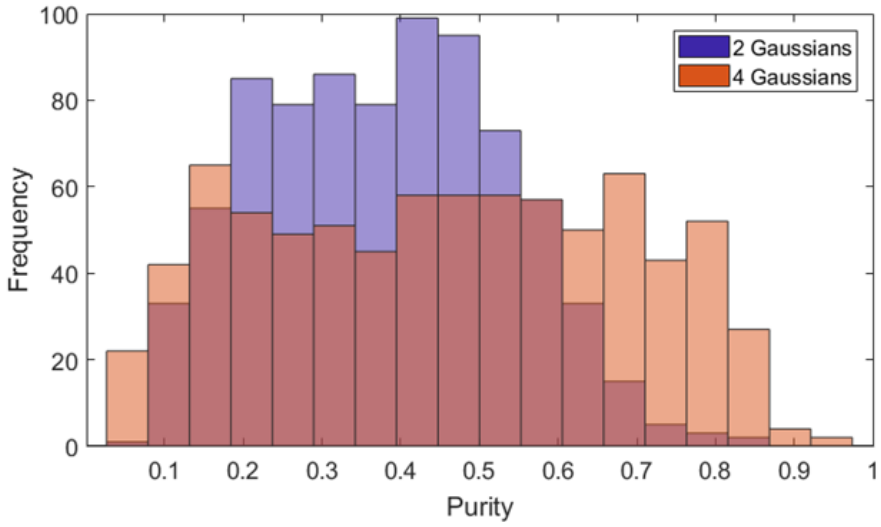

Figure 9. Distribution of purity using the two-Gaussian and four-Gaussian models when only the data from the main diagonal is used.

8. Comparison of KRAKEN and Mixed-FROG

KRAKEN and Mixed-FROG are the two main protocols for measuring the quantum state of photoelectrons. Mixed-FROG was suggested in 2015 [33] and was implemented experimentally in 2020 [30].

In mixed-FROG, an attosecond pulse train ionizes the target and a strong IR pulse drives multiple continuum-continuum transitions, coupling the different photoelectron peaks in the spectrum. In [30], this was achieved using an IR intensity of 6×10^{12} W/cm^2. A spectrogram is obtained by scanning the delay between the XUV and IR over the whole cross-correlation trace. Due to the interference between quantum paths involving many continuum-continuum transitions, the photoelectron signal oscillates at high frequencies (up to 6ω in [30], where ω is the angular frequency of the IR laser). The photoelectron quantum state is obtained by applying a mixed state principal component generalized projection algorithm to the spectrogram. In [30], the photoionization process in the presence of the XUV field and the strong IR pulse was modeled using the strong field approximation. The purity of the photoelectron quantum state measured in neon gas in [30] was 0.11. No error bars on the purity were given, but the error of the reconstruction was monitored to ensure convergence of the reconstructed density matrix. To explain the low purity of the measured quantum state, different sources of decoherence were explored: temporal jitter, attochirp fluctuations, and limited spectrometer resolution. The authors concluded that the main sources of decoherence in their measurements were the temporal jitter and the spectrometer response. The effect of ion-photoelectron entanglement in neon was not investigated.

In KRAKEN, an XUV pulse ionizes the target and two weak IR pulses at different wavelengths are used to induce interference between different energies within populated photoelectronic states. A photoelectron spectrogram is obtained by scanning the delay between the XUV and IR. In principle, the whole cross-correlation trace does not need to be measured. In these measurements,

the IR pulse must be weak ($\approx 10^{11}$ W/cm^2) to ensure that only one IR photon is absorbed. From the oscillations in the spectrogram, a subdiagonal of the density matrix is directly obtained. These measurements are repeated for different values of $\delta\omega$ in order to map out the density matrix. If the number of measurements is large enough and the values of $\delta\omega$ match the grid used for plotting the density matrix, in principle, no further processing is needed. In practice, it is very challenging to perform enough measurements, and a Bayesian estimation technique can be used to retrieve the most likely density matrix underlying the measured data as described above. In this work and the previous theoretical study [35], the effect of different sources of decoherence have been investigated: noise, XUV and IR intensity fluctuations, and limited spectral resolution. The main potential sources of decoherence that have been identified are noise and limited spectral resolution. The energy spread of the photoelectrons reconstructed with KRAKEN has been until now limited to a few hundred meV. Although technically challenging, KRAKEN could be applied to photoelectrons populating a wider superposition of continuum states. In that case, like mixed-FROG, temporal jitter of a several tens of attoseconds could introduce experimental decoherence.

The main advantage of mixed-FROG is that it is relatively easy to implement experimentally since the experimental setup is essentially the same as for measurements using the reconstruction of attosecond beating by interference of two-photon transitions, a standard measurement technique in attosecond physics [10]. The drawbacks are that it relies on a specific model to retrieve the density matrix and that it requires high IR intensities that can affect the physics of photoionization [63].

The main advantage of KRAKEN is that the IR can be treated perturbatively and that, in principle, it gives direct access to the photoelectron density matrix. In the case where the density of measurement is not large enough, a model must be used to reconstruct the density matrix. This model does not make any assumptions about the physics of photoionization. Instead, it is a purely mathematical optimization that tries to capture the geometric shape described by the density matrix elements. The drawbacks are that it requires performing multiple measurements and that it is experimentally more demanding than mixed-FROG measurements, requiring extended spectral tuning and shaping of the IR probe pulse. Additionally, the IR pulses must be spectrally narrow, i.e., temporally long, to limit finite pulse effects [60]. It can then be challenging to achieve high enough IR intensity in the interaction region to observe two-photon ionization.

In the measurements reported here, we obtain purities that are higher than that reported in the pioneering work of Bourassin-Bouchet and coworkers [30]. We attribute this to two important aspects. First, the spectral resolution of our spectrometer is a bit higher than that used in Ref. [30]. Additionally, we further included the spectrometer response in the Bayesian estimation algorithm to correct for this known source of decoherence. Second, the measurements presented in this work are much less sensitive to temporal jitter, owing to the slower period of oscillation in our measurements.

9. Experimental decoherence

The purity of the photoelectron quantum state can be lower than one for two different reasons. As discussed in the main text, performing incomplete measurements on an entangled system can lead to a loss of purity. Experimental decoherence can also reduce the photoelectron purity, as originally

discussed by Bourassin-Bouchet *et al.* [30]. In our measurements, in order to disentangle the effect of experimental decoherence and ion-photoelectron entanglement, we performed consecutive measurements in helium and argon atoms. In helium, theory predicts that in the absence of experimental decoherence, the photoelectron purity should be equal to one. Therefore, the measurements in helium allow us to quantify the degree of experimental decoherence in our measurements.

If we do not account for the finite spectrometer resolution, we obtain a photoelectron purity of $\gamma \approx 0.87 \pm 0.06$ in helium and $\gamma \approx 0.58 \pm 0.03$ in argon. This shows that our measurements are sensitive to experimental decoherence and in argon, the reduced purity cannot only be attributed to ion-photoelectron entanglement. The physical origin of experimental decoherence can be:

- Temporal jitter

In our work, the photoelectrons cover a small range of energies so that the fastest oscillations are of the order of tens of femtoseconds while the temporal jitter is of the order of tens of attoseconds, i.e. three orders of magnitude smaller. As a result, the effect temporal jitter is negligible in our work.

- Limited spectral resolution of the photoelectron detector

The finite resolution of the MBES is an important limitation. However, the spectrometer response function can be measured and included in the Bayesian optimization algorithm. The density matrix in Figs. 3B and 4B of the main manuscript are corrected for the spectrometer induced decoherence. This accounts for the limited time-of-flight resolution of the detector as well as volume averaging effects in the interaction region.

- Dark counts in the photoelectron detector / noise

This effect is relatively small for the measurement of the coherences since the signal is modulated at the frequency $\delta\omega$, acting as a lock-in detection scheme. In contrast, the measurement of the populations is much more sensitive to noise. Here we use a mechanical chopper in the probe arm that blocks the IR every other laser shot, providing a background measurement that is subtracted from the XUV+IR signal.

- Fluctuations of the amplitude and phase of the XUV or IR pulses

Fast fluctuations of the order of a few percent do not significantly affect the purity of the photoelectrons as discussed in Ref. [30]. Slow fluctuations over the measurement of a spectrogram can affect the low beating frequencies. The XUV and IR intensity was continuously monitored during the measurement and no indication of slow fluctuations was found.

- Slow experimental drifts during a measurement

As discussed above, slow experimental drifts can lead to an enhancement of the populations and subdiagonals closest to the main diagonal. However, Supplementary Fig. 7 shows that this does not seem to be the case in our measurements.

- Partially coherent XUV or IR pulses

If the light sources are not fully coherent, the amplitude of the oscillations can be reduced, leading to populations that are much larger than the coherences. While we have observed in some measurements (not presented in this manuscript) that amplified spontaneous emission in the laser amplification chain can affect KRAKEN measurements, in the measurements presented in the manuscript, there is no hint of this effect. Note that the XUV pulses are expected to be highly coherent since only the coherent part of the IR will be able to drive high harmonic generation.

When we account for the finite spectral resolution of the MBES, we find purities of $\gamma = 0.94 \pm 0.06$ in helium and $\gamma = 0.65 \pm 0.02$ in argon. The very high purity in helium, compatible with that of a pure state, indicates that the main source of experimental decoherence was the finite spectral resolution of the measurements. In these conditions, the reduced purity in argon can be attributed to the ion-photoelectron entanglement, which can be quantified by computing the concurrence as described in the main text.

10. Ion-photoelectron entanglement in argon and loss of coherence

We start from the general wave function describing the ion+photoelectron system

$$|\Psi\rangle = \sum_{j,\alpha} \int d\epsilon \, c_{j,\alpha}(\epsilon) |\phi_j\rangle \otimes |\psi_{\alpha,\epsilon}\rangle,$$

where $|\phi_j\rangle$ are the ionic states and $|\psi_{\alpha,\epsilon}\rangle = |\alpha\rangle \otimes |\epsilon\rangle$ are the continuum states characterized by the energy ϵ and a set of quantum numbers α necessary to uniquely describe the continuum states (spin, angular momentum). In general, experiments cannot measure all degrees of freedom of the total system. In order to characterize the reduced quantum system that is addressed in the experiments, we use the density matrix formalism. The density matrix describing the total system, which is pure (no interaction with the environment), is given by $\rho = |\Psi\rangle\langle\Psi|$. We will distinguish between two different sets of experiments, experiments that focus on measuring the ion, by measuring the ion momentum distribution or attosecond transient absorption, and experiments measuring the photoelectron, be it angle-resolved or angle-integrated.
For experiments measuring the ions, the reduced density matrix is given by

$$\begin{aligned}\rho_{ion} &= \sum_{\alpha} \int d\epsilon \, \langle \psi_{\alpha,\epsilon} | \rho | \psi_{\alpha,\epsilon} \rangle \\ &= \sum_{\alpha,j,k} \int d\epsilon \, c_{j,\alpha}(\epsilon) c^*_{k,\alpha}(\epsilon) |\phi_j\rangle\langle\phi_k|,\end{aligned}$$

while for experiments measuring photoelectrons the reduced density matrix is given by

$$\begin{aligned}\rho_{elec} &= \sum_{j} \langle \phi_j | \rho | \phi_j \rangle \\ &= \sum_{j,\alpha,\beta} \int d\epsilon_1 d\epsilon_2 \, c_{j,\alpha}(\epsilon_1) c^*_{j,\beta}(\epsilon_2) |\psi_{\alpha,\epsilon_1}\rangle\langle\psi_{\beta,\epsilon_2}|.\end{aligned}$$

If, as in this work, only the photoelectron kinetic energy is measured, one needs to further trace over α, leading to

$$\rho_{elec} = \sum_{j,\alpha} \int d\epsilon_1 \, d\epsilon_2 \;\; c_{j,\alpha}(\epsilon_1) c^*_{j,\alpha}(\epsilon_2) |\epsilon_1\rangle\langle\epsilon_2|.$$

For ions, in order to observe coherences between different states it necessary that the electrons associated with different ionic states have quantum numbers α in common and that the photoelectron spectra partially overlap, i.e. there is an energy ϵ_0 and a set of quantum numbers α_0 such that both $c_{j,\alpha_0}(\epsilon_0)$ and $c^*_{k,\alpha_0}(\epsilon_0)$ are non-zero. This is what was observed in Ref. [64] and further discussed, for example, in Refs. [25,27]. When the ionization pulses are very short, the photoelectron spectra are broad, ensuring a large overlap between the photoelectron spectral amplitudes associated to the different ionic states. In this case, even after tracing over the photoelectron degrees of freedom, a high degree of coherence can be observed between the different ionic states as illustrated [64].

For photoelectrons, in order to observe coherence between two photoelectron states, it is necessary that the ionic state is the same, or, at least, that the photoelectron states are associated to two non-orthogonal ionic states. In the case of argon, the $3p^5\ ^2P_{1/2}$ and $3p^5\ ^2P_{3/2}$ ionic states are orthogonal so that, after tracing of the ionic degree of freedom, it is impossible to observe coherence between photoelectronic states associated to different final ionic states.

In principle, one can perform angle-resolved photoelectron measurements. When detecting a photoelectron at a specific emission angle, coherence (i.e., interference) between photoelectronic states with different angular momenta (but associated to the same ionic state) is possible since they are not orthogonal in the measurement basis (momentum basis). However, when averaging over all emission angles, different partial waves will add incoherently in the total photoionization yield due to the orthogonality of spherical harmonics. The effect of angular integration on the photoelectron quantum state has been discussed in [24]. In general, for non-resonant photoionization over a small energy range, angular integration will affect the purity of the reduced state.

Finally, we provide an explanation for the purity value obtained in argon. We start from Eq. (2) in the main manuscript

$$|\Psi\rangle = \frac{1}{\sqrt{3}} \left|\phi_{1/2}\right\rangle \otimes \left|\psi_{\frac{1}{2}}\right\rangle + \sqrt{\frac{2}{3}} \left|\phi_{3/2}\right\rangle \otimes \left|\psi_{3/2}\right\rangle,$$

By expanding $\left|\psi_{1/2}\right\rangle$ into the energy basis:

$$|\Psi\rangle = \frac{1}{\sqrt{3}} \left|\phi_{1/2}\right\rangle \otimes \int d\epsilon \; b_{1/2}(\epsilon) |\epsilon\rangle + \sqrt{\frac{2}{3}} \left|\phi_{3/2}\right\rangle \otimes \int d\epsilon \; b_{3/2}(\epsilon) |\epsilon\rangle.$$

The distributions $b_j(\epsilon)$ are centered at different kinetic energies and depend on the spectrum of the ionizing pulse and the energy-resolved photoionization matrix elements. Because the two distributions are different the above state is entangled. However, in the limit where the ionizing radiation is much broader that the spin-orbit splitting, we get $b_{1/2}(\epsilon) \approx b_{3/2}(\epsilon)$ and we recover a separable state. From this is it clear that the degree of entanglement depends on the spectral width of the pulses compared to the spin-orbit separation.

The reduced density matrix ρ_{elec} can be expressed as $\rho_{elec} = \frac{1}{3}\rho_{1/2} + \frac{2}{3}\rho_{3/2}$, where ρ_j is the reduced photoelectron density matrix that would be measured in only $|\phi_j\rangle$ was populated (or if the electrons and the ionic state could be measured in coincidence). To a good approximation, $b_{3/2} \approx b_{1/2}(\epsilon - \Delta\epsilon_{SO})$, yielding the following expression for the purity:

$$\gamma = \frac{5}{9} + \frac{4}{9}\left|\int b_{1/2}^{*}(\epsilon) b_{1/2}\,(\epsilon - \Delta\epsilon_{SO}) d\epsilon\right|^2 .$$

This expression shows that the purity of the photoelectron depends on the degree of overlap between the distributions $|b_j(\epsilon)|$, the minimal purity possible (in the absence of experimental decoherence) being $\gamma = 5/9 \approx 0.556$. In our experiments, the partial overlap of the two distributions leads to an increased purity of 0.65.

11. Broad perspective on attosecond science and quantum information

In our work, we show that applying the tools from quantum information science to photoionization opens new perspectives, allowing, for example, the rigorous study of electronic decoherence processes in light-matter interaction. This development is part of a broader field of research at the interface of attosecond physics and quantum science that has emerged at the turn of this decade. This new field can be separated in four research lines:

- Study of quantum correlations and entanglement in fragmentation processes such as photoionization and photodissociation [29,30,46]
- Generation and detection of non-classical photonic states with very large numbers of photons [52-57]
- Generation and detection of quantum states and phases in strongly correlated materials [65,66]
- Generation and detection of topological order and quantum topological properties [67,68, 69]

These lines of research are not orthogonal to each other and we can expect that in the future the different research topics will merge, resulting in a more holistic approach to the study of quantum effects in ultrafast light-driven processes in matter.

References

59. D. Busto, S. Zhong, J. M. Dahlström, A. L'Huillier and M. Gisselbrecht *Ultrafast Electronic and Structural Dynamics* (Singapore: Springer Nature Singapore) chap 1, pp 1– 43 (2024)

60. A. Jimenez-Galán, L. Argenti, F. Martín, *Two-photon finite-pulse model for resonant transitions in attosecond experiments*, Phys. Rev. A **93**, 023429 (2016)

61. K. Varjú, *et al.*, *Frequency chirp of harmonic and attosecond pulses*, J. Mod. Opt. **15**, 379-394 (2005)

62. M. D. Hoffman, A. Gelman, *The No-U-Turn Sampler: Adaptively Setting Path Lengths in Hamiltonian Monte Carlo*, J. Mach. Learn. Res. **15**, 1593-1623 (2014)

63. C. Ott *et al.*, *Lorentz Meets Fano in Spectral Line Shapes: A Universal Phase and Its Laser Control*, Science **340**, 716-720 (2013)

64. E. Goulielmakis *et al.*, *Real-time observation of valence electron motion*, Nature **466**, 739-743 (2010)

65. J. Alcalà, U. Bhattacharya, J. Bigert, *High-harmonic spectroscopy of quantum phase transitions in a high-Tc superconductor*, Proc. Natl. Acad. Sci. **119**, e2207766119 (2022)

66. R. E. F. Silva, I.V. Blinov, A. N. Rubtsov, O. Smirnova, M. Ivanov, *High-harmonic spectroscopy of ultrafast many-body dynamics in strongly correlated systems*, Nat. Photon. **12**, 266 (2018)

67. R. E. F. Silva, Á. Jimenez-Galán, B. Amorim, O. Smirnova, M. Ivanov, *Topological strong-field physics on sub-laser-cycle timescale*, Nat. Photon. **13**, 849 (2019)

68. Á. Jiménez-Galán, R. E. F. Silva, O. Smirnova, M. Ivanov, *Lightwave control of topological properties in 2D materials for sub-cycle and non-resonant valley manipulation*, Nat. Photon. **14,** 728 (2020)

69. A. Chacón *et al.*, *Circular dichroism in higher-order harmonic generation: Heralding topological phases and transitions in Chern insulators*, Phys. Rev. B **102**, 134115 (2020)